High-speed Real-time X-ray Image Recognition based on a Pixelated SiPM Coupled Scintillator Detector with Radiation Photoelectric Neural Network Structure

Kai Meng, Pin Gong *, Dajian Liang, Zeyu Wang, Zhimeng Hu, Peng Wang, Cheng Zhou, Xiaoxiang Zhu, Xiaobin Tang

***Abstract*—In monitoring scenarios for material processing and accident status evaluation, high-speed X-ray imaging at the microsecond or even nanosecond level is utilized. Real-time, long-term high speed x-ray image processing is difficult to realize with existing technology; main limitations are detector system structure and the need for high-speed transfer and storage of a large number of digital signals. Therefore, this paper proposes an irradiated photoelectric neural network for high-speed real-time X-ray image recognition based on a pixelated radiation detector. We use a SiPM coupled scintillator to realize this pixelated radiation detector. The weights of a neural network are mapped to the bias voltage of SiPM pixels, so that the SiPM array itself constitutes a neural network. By analyzing the output signals of an array of SiPMs, X-ray image can be recognized in real-time. The whole process does not involve complicated digital circuits and digital signal processing. The feasibility of the method was verified by experiments. As the initial stage of the study, we achieved an X-ray image recognition speed of 500,000 frames per second. The simplicity and innovation of this detector fully demonstrate its future application prospects. It is especially suitable for applications that require long-term continuous monitoring of radiographic images and immediate feedback of results, such as online monitoring of high-speed material processing, observation of the cosmic environment and other continuously changing scenes of X-ray images.**

***Index Terms*—SiPM, Real-time image recognition, X-rays, Photoelectric neural networks**

I. Introduction

THERE are demands to get internal information of objects in a very short time in laser processing defect observation [1][2], battery thermal runaway observation [3], fuse blowing observation [4], and ballistic analysis [5]. At present, offline analysis by using high-speed X-ray imaging is the main observation method in these demands. The imaging speed of most high-speed X-ray imaging is in the microsecond to millisecond scale of a single X-ray image [3][6]. On the one hand, the imaging speed of X-ray imaging has much room for improvement, so there is much research on this topic [6][7]. On the other hand, even though the single imaging time can be controlled to nanoseconds, there are still limitations in the continuous imaging for a long time, which makes it difficult to monitor the exact timing and phenomenon outside of the predetermined time frame.

In fact, getting images to achieve such observation needs is unnecessary if there are enough technical means. Because image analysis is only a medium to get the information of the objects' location, material's pore size, accident generation time, etc. Existing methods to get this information are mainly indirect monitoring like sound and ultrasonic [8][9]. X-ray image is a more direct approach, but it can only be used for off-line analysis. The ultimate goal is to extract useful information from the image. Therefore, it is necessary to bypass the X-ray imaging step and develop new methods or detectors which can sense X-ray image information in real-time on a smaller time scale for long-term observation and can feed back observation results directly.

By analyzing the current high-speed X-ray imaging detector system, it can be found that the limitations of the speed of X-ray imaging are caused by data explosion which produces the need to process and store a large number of digital signals in a short time. A complete high-speed X-ray imaging system includes functional modules such as a scintillation screen, image sensors (CCD/COMS), signal readouts, signal processing, and image reconstruction. And, to handle complex images, various image recognition algorithms have been developed in recent years as follow-up modules of X-ray images[10][11]. Under this imaging system structure, the main

This work was supported by the Primary Research and Development Plan of Jiangsu Province (Grant No. BE2022846), and the Fundamental Research Funds for the Central Universities (Grant No. NC2022006).

Kai Meng, Dajian Liang, Zeyu Wang and Zhimeng Hu are with the Department of Nuclear Science and Technology, Nanjing University of Aeronautics and Astronautics, Nanjing 211106, China (e-mail: mengkai@nuaa.edu.cn; liangdajian@nuaa.edu.cn; wangzeyu@nuaa.edu.cn; huzhm21@nuaa.edu.cn).

Pin Gong * and Xiaobin Tang are with the Department of Nuclear Science and Technology, Key Laboratory of Nuclear Technology Application and Radiation Protection in Astronautics, Ministry of Industry and Information Technology, Nanjing University of Aeronautics and Astronautics, Nanjing 211106, China (e-mail: gongpin@nuaa.edu.cn; tangxiaobin@nuaa.edu.cn).

Peng Wang is with the School of Environmental and Biological Engineering, Nanjing University of Science and Technology, Nanjing 210094, China (e-mail: wp739130046@nuaa.edu.cn).

Cheng Zhou and Xiaoxiang Zhu are with the Jiangsu Nuclear and Radiation Safety Supervision and Management Center, Nanjing 210019, China (e-mail: flyingzc@163.com; zhu.jsre@163.com).

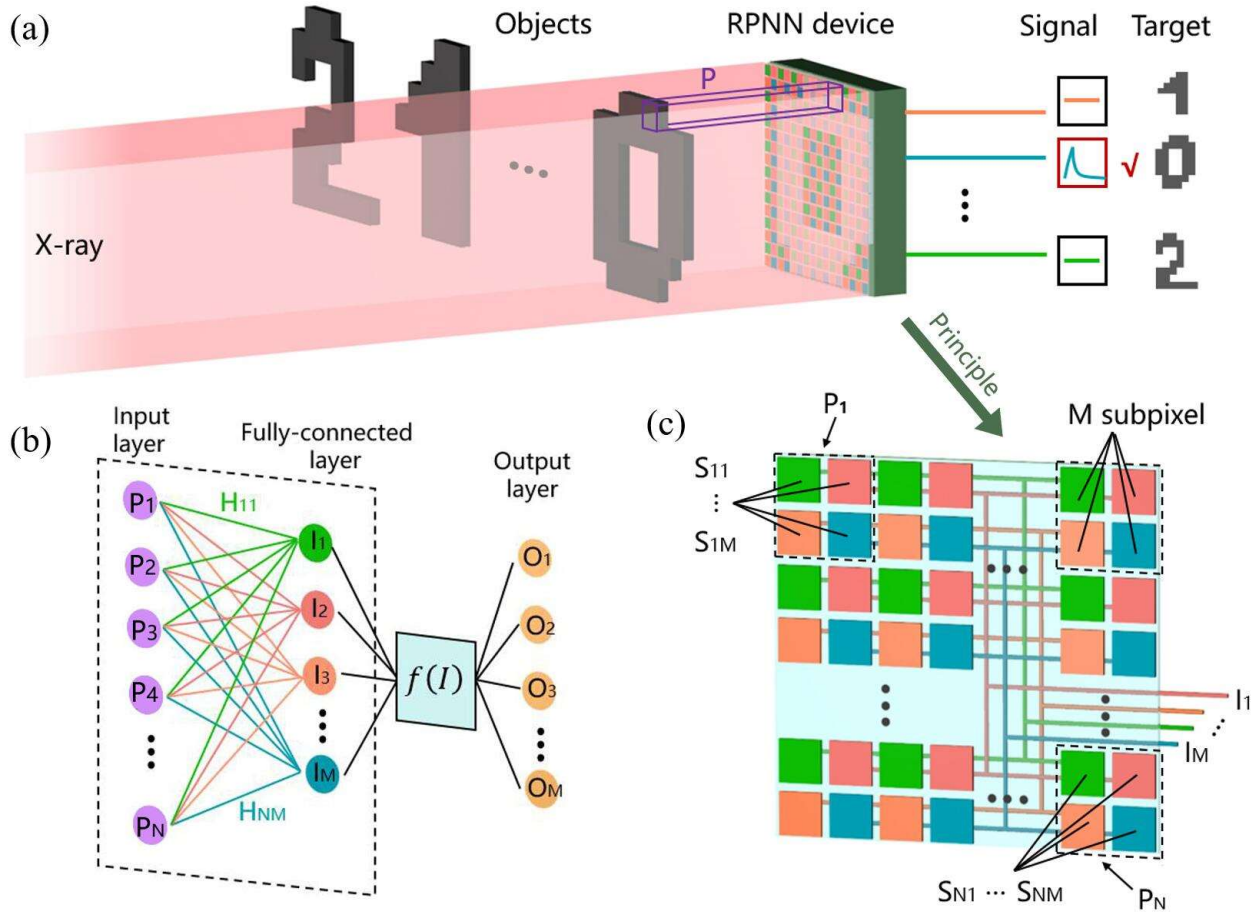

Fig. 1. Schematic of the radiation photoelectric neural networks detector. (a). The basic implementation process of the RPNN. X-ray irradiates the objects and the objects will be recognized according to the output signal of the RPNN detector. (b). The architecture of RPNN as a classifier. And $f(I)$ represents the off-chip output activation function. (c). The structure of the detector array. Each part is consistent with the meaning of the same color in (b). M subpixels S constitute an image pixel P, and S of the same color are connected in parallel to form an output signal, resulting in a total of M output signals.

means to improve imaging speed is to develop scintillators with higher luminous efficiency and faster decay time [6], pixel array detectors (PADs) with faster imaging speeds, and signal readout circuits with higher frequency [12][13][14], or optimizing the optical design [15]. Advanced high-speed X-ray imaging detector systems through this approach has been able to capture single images within one hundred nanoseconds. Although the theoretical imaging speed can reach 10 million frames per second, the finite number of sequential images makes it incompatible with continuous imaging for long periods of time. And with the image recognition algorithm used after image storage, the speed of obtaining information on images will be much slowed down. As a result, many studies could only take a few key frames into X-ray images for offline analysis [1][2].

Predictably, the performance of high-speed X-ray imaging is difficult to be improved on the existing basis, as the traditional von Neumann system by Moore's law approaches its physical limits. So now, significant efforts are being devoted to developing systems that are different from traditional optical imaging methods [16][17], especially in some imaging systems that imitate biological structures [18-21], which are expected to overcome the problems of data storage and imaging speed. This provides an attractive development direction for improving the speed of acquiring X-ray image information.

In this study, a high-speed real-time X-ray image recognition system based on a pixelated radiation detector is tested for the first time, and the detector constitutes an ANN that can sense and recognize projected X-ray images at the same time. We use a silicon photomultiplier (SiPM) coupled scintillator to realize this pixelated radiation detector. The overall structure of the detector is simple, without complicated digital signal processing and storage circuits, and the X-ray image objects can be recognized by the detector's output signal.

II. Principles

Here we will show the basic implementation of the detector. We use a SiPM coupled scintillator to build the detector called radiation photoelectric neural networks (RPNN). When X-rays irradiate objects which need to be recognized, the X-ray passing through the object will show a certain X-ray image. The RPNN detector has several output signal channels. And the channels of this RPNN detector will output a specific signal after detecting the X-ray image. Therefore, the object can be recognized by this signal, as shown in figure 1(a).

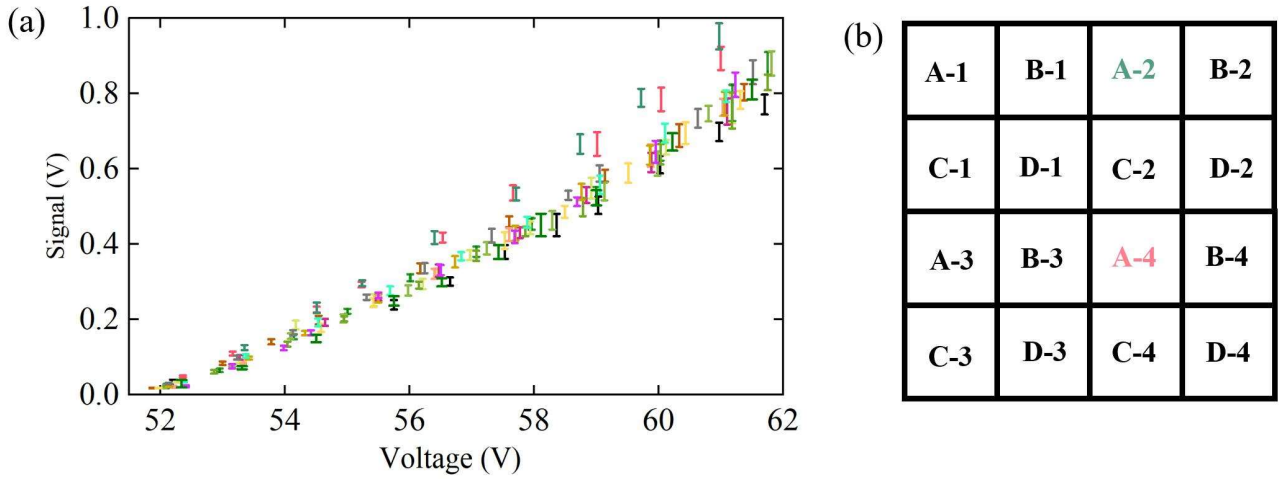

Fig. 2. (a) Relationship between output and bias voltage of 16 pixels; (b) Location distribution of 16 pixels.

Figure 1(c) illustrates the schematic of the RPNN detector, in which each detector pixel represents a subpixel called *S*, and *M* subpixels constitute an image pixel *P*. For an image with *N* pixels, *M*×*N* subpixels are present on the detector array. Similarly, figure 1(b) shows the ANN that is used to implement image recognition in the detector. The input layer is composed of *N* input image pixels *P*, each of which is summed in the fully connected layer after weight H_{NM} calculation, and then reaches the output layer which consists of *M* output nodes through a nonlinear activation function $f(I)$. That makes the number of weights $H = M \times N$ which is the same as the number of subpixels on the detector array. Correspondingly, there are *M* output current channels in the detector array to equal with output layer nodes in the ANN. By paralleling the output signals of the same color of S_{NM} in the array according to Kirchhoff's law, the output current signal I_M can be analogous to the summation process of the ANN after the fully connected layer. Therefore, through mapping the weight H_{NM} of the ANN to the detector array, the ANN in figure 1(b) can be transferred to the RPNN detector, to directly realize the object image recognition.

A SiPM is a photomultiplier device, whose output signal amplitude is influenced by its bias voltage [22], and a higher bias voltage corresponds to a larger output signal amplitude for a given input. X-rays are converted into optical light of a specific wavelength by the scintillator and then the current is generated by SiPM. Setting the bias voltage of each SiPM pixel individually can produce current signals of different amplitudes when the input remains the same. We calibrated the relationship between the output signal amplitude of each SiPM's pixel and the bias voltage, as shown in figure 2. The ordinate is voltage because we used an amplifier and observed it on an oscilloscope, which made an I-V conversion process. As the voltage increases, the amplitude of the output signal increases almost linearly. The trend of 16 pixels signals is consistent, with no bad pixels. It could be seen that only two pixels were slightly different from all pixels. They are A-2 and A-4. This may be caused by the manufacturing difference. Then, by establishing the corresponding relationship between SiPM bias and neural network weight, the above ANN can be realized on the SiPM array. This correspondence requires only a linear mapping of weights and bias voltage. In this situation, SiPM acts as a single-layer perceptron.

III. RPNN Training

To verify the principle, a 4-input, 4-category network was constructed and four 2×2 patterns called *A*, *B*, *C*, and *D* were set in the computer as shown in Figure 3(a), and the bright and dark levels were the same for every pattern in original. To ensure that the training is close to the real situation, and to augment the amount of training data, the Gaussian noise and crosstalk noise that would be generated in the actual process were considered. Noise with signal-to-noise ratios (SNRs) of 5, 3, and 2 were added respectively in the four patterns, thereby generating 400 input images (100 images per pattern) for every SNR. Weights were constrained between 0 and 1 during training and one-hot encoding was adopted, which means only one output neuron was activated for each pattern.

The softmax function was selected as the activation function of the output node as

$$f_m(I) = \frac{e^{\xi I_m}}{\sum_{k=1}^{M} e^{\xi I_k}} \tag{1}$$

where $\xi = 10^6 A^{-1}$ is the scaling factor that ensures all values of the activation function $f_m(I)$ reach a standard probability distri bution and their sum is 1. The loss function in training used the cross-entropy function which has good performance in classification problems:

$$L = -\frac{1}{M}\sum_{m=1}^{M} y_m \log[f_m(I)] \tag{2}$$

where y_m is the label (0 or 1) and *M* is the classification number, for $M = 4$ in this paper. The initial values were obtained by pseudo-random numbers, and the weights were updated by backpropagation of stochastic gradient descent in each training session, with a learning rate of 0.1 [23]. Given the simplicity of the network and to achieve the best training result as soon as possible, a learning rate attenuation coefficient was set to 0.99.

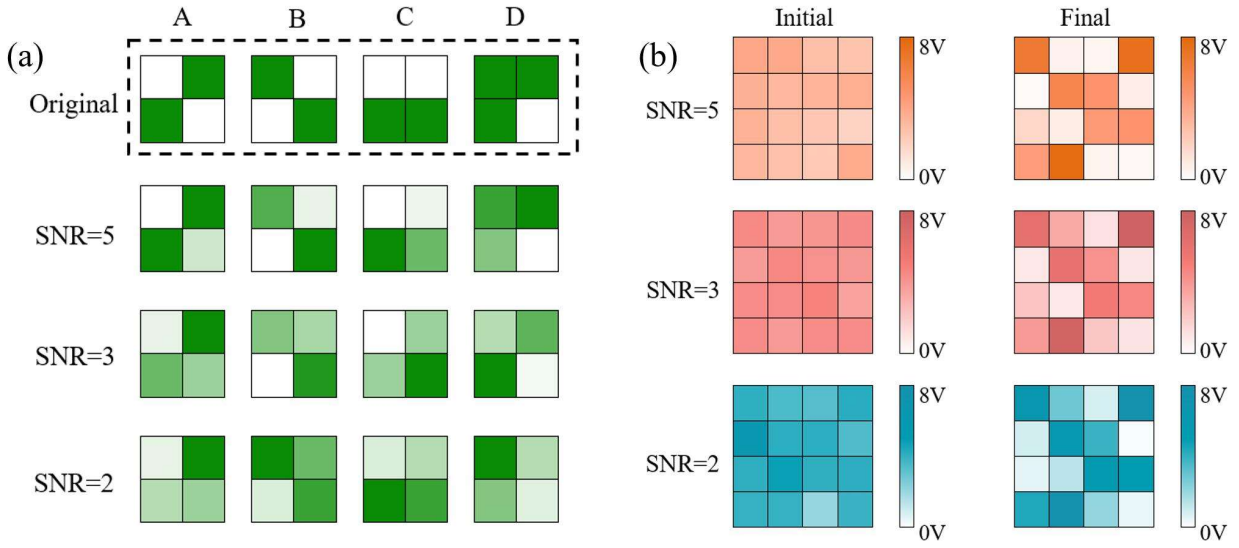

Fig. 3. RPNN training images. (a) *A, B, C, D*. Four kinds of training original images and input images with SNR of 5, 3, and 2 respectively; (b) Initial SiPM pixel's bias voltage and trained pixel's bias voltage (overvoltage) under different noise levels.

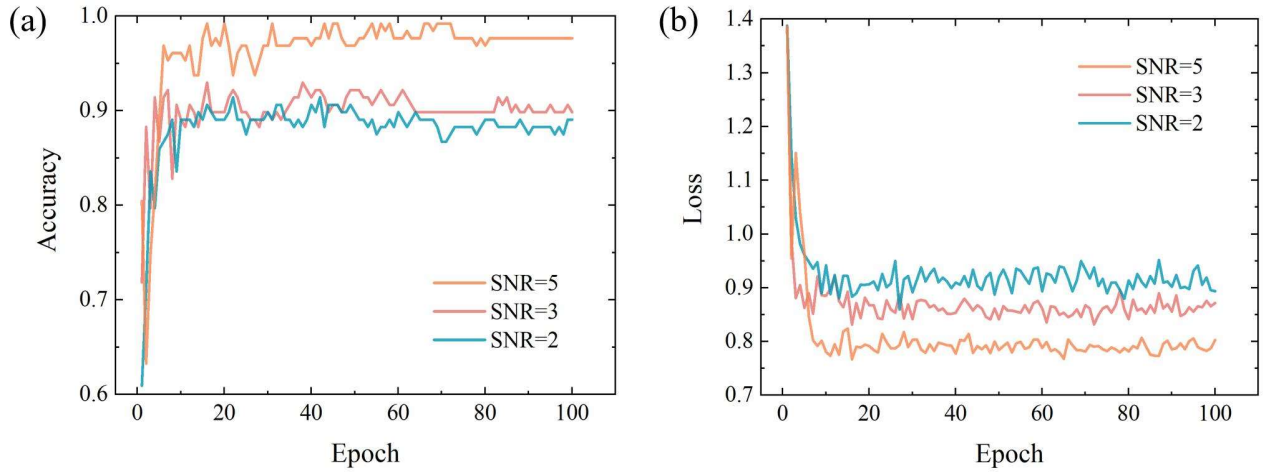

Fig. 4. Training curve. (a) Accuracy of image recognition under different noise levels; (b) Convergence of loss function under different noise levels.

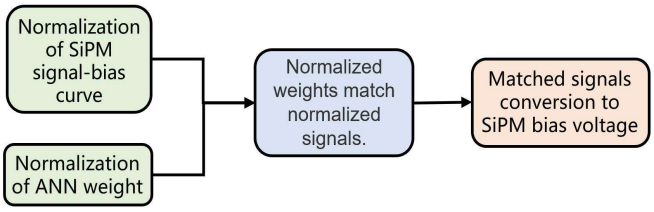

Fig. 5. Mapping relationship between ANN weight and SiPMs' bias voltage.

All images are divided into a training set and a test set with a ratio of 8:2 to ensure that the network is not over-fitting.

Figure 4(a) and 4(b) show the curves of image recognition accuracy and loss convergence curve under different SNRs, from initialization to epoch 100. No matter the amount of noise, the network tends to converge in the first 20 epochs, and then stabilize, while the accuracy increases with the decrease in noise by training. Under a high noise level, the accuracy fluctuates more. The accuracy dropped to almost below 90% under SNR = 2, but the recognition accuracy can be stably maintained above 97% under SNR = 5. Also, due to the non-negative condition of weight, the loss value converged to about 0.79, 0.85, and 0.91 under different noises.

After training, we normalized the output signal between 0 and 1, and the normalized output signal is used to correspond to the weights, to realize the mapping from weight to bias, as shown in figure 5. Figure 3(b) shows the initial SiPM bias voltage (exceeding breakdown voltage) under different noise levels and the final bias voltage which neural network weights are mapped after training. The darker color indicates higher overvoltage. Given that excessive voltage greatly increases the crosstalk probability and dark current in practice, the maximum voltage limit was set to 8 V above overvoltage. The voltage between pixels was more unevenly distributed compared with that before training. Although the bias voltage distribution is similar under these three noise levels, the voltage difference between pixels is more obvious with the higher SNR.

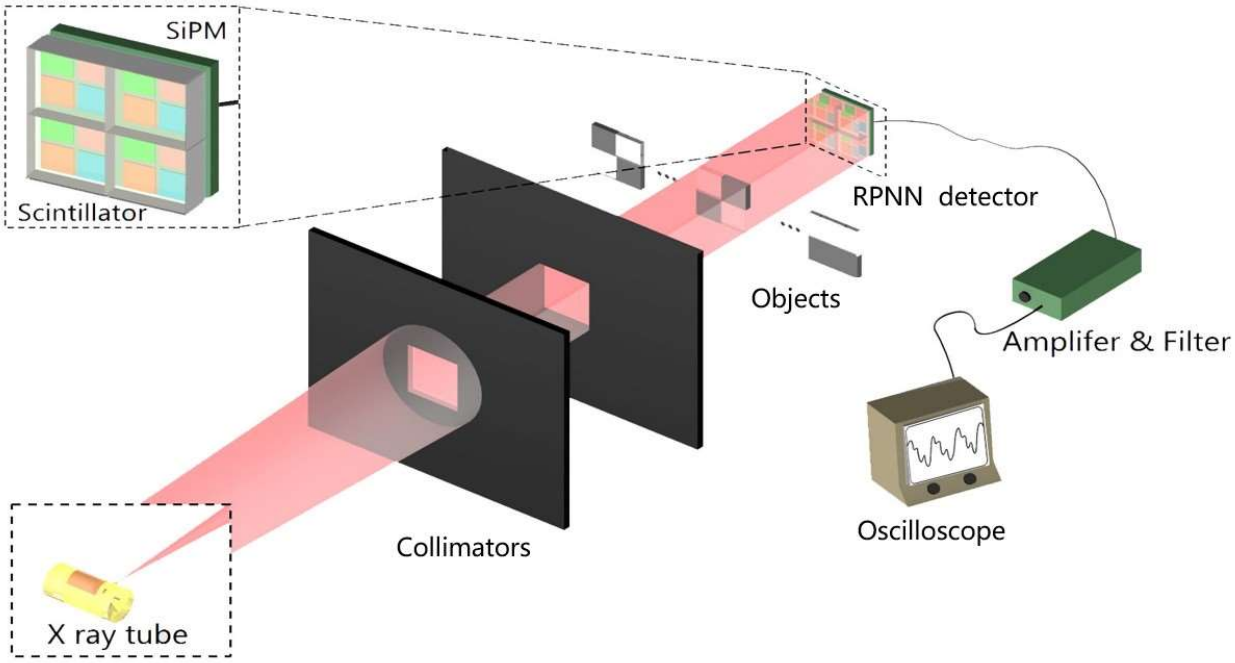

Fig. 6. Experimental scheme of RPNN.

IV. Experiments

After the network weights were obtained and mapped to SiPM bias voltage, the actual experimental effect can be tested by the actual device. The experiment used a groove-shaped grid-controlled modulated X-ray tube developed by our laboratory, which can stably generate square-wave X-ray pulses with a frequency from 1 kHz to several MHz [24]. The overall structure of the experimental device is shown in Figure 6. The emitted X-ray energy from this tube was mainly distributed around 10 keV at 50 kV tube voltage. The parallel X-ray is required because there is no additional focusing structure on the detector, and the projected image needs to have the same size as the detector. Two-layer collimators made of lead were arranged at a distance of 30 cm from the X-ray source to obtain a parallel X-ray beam. The thickness of each collimator was 1 mm, and the distance between them was 5 cm. The size of the collimating hole was 25 mm × 25 mm, and it was consistent with the subsequent object size that needs to be recognized. The X-rays after passing through the collimator reached the object through 3 cm of air, and the pattern was the same with the network training in Figure 3(a). To obtain a clear and obvious pattern, tungsten, which transmittance is less than 1% at 10 keV X-ray and 1 mm thickness, was used. Each tungsten block (image pixel) had a side length of 12.5 mm and a thickness of 1 mm, forming a 2×2 image array, which was placed 2 cm in front of the detection array. To improve the image recognition speed, and reduce the time delay of the whole process, LYSO crystal with fast luminescence decay time (about 43 ns) and high light yield (about 70% relative to NaI) was selected. The overall crystal size was 25 mm×25 mm × 10 mm, which was consistent with the coupled SiPM array, and it was divided into uniform 4×4 pixels. Its pixel size was 6 mm ×6 mm, and there was a 0.2 mm $BaSO_4$ reflective layer between pixels. This crystal was

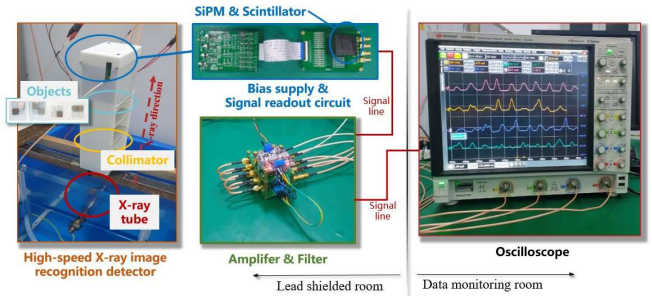

Fig. 7. Experiment setup of RPNN. The X-ray tube was soaked in insulating oil to provide a vacuum environment. The white shell provided the physical support of the components. Components were seated in the lead-shielded room except for the oscilloscope.

combined with 4×4 array SiPM by the optical couplant. The SiPM was the S13361-6050 series from Hamamatsu with low crosstalk and dark counts. The photosensitive area for each SiPM pixel was 6 mm × 6 mm and the distance between SiPM pixels was also 0.2 mm.

Before the experiment, the relationship between the output signal of each pixel of SiPM and the bias voltage was tested, as shown in figure 2. We found that when the bias voltage exceeded 8 V above the breakdown voltage (the total bias voltage was about 60 V) of each pixel, the amplitude of the output signal fluctuated more due to noise such as dark counting and crosstalk noise. It would affect the subsequent judgment of the output signal amplitude. Therefore, we set the upper limit of the voltage to 8 V above the breakdown voltage, to obtain a stable output signal. Then we connected the SiPM array pixels into four output channels, just like the same colors shown in figure 1(c). The four output signals were amplified by a self-developed integrated small-sized preamplifier and a filter, which were used to amplify useful signals and remove high-frequency noise in the signal transmission process. Then, the

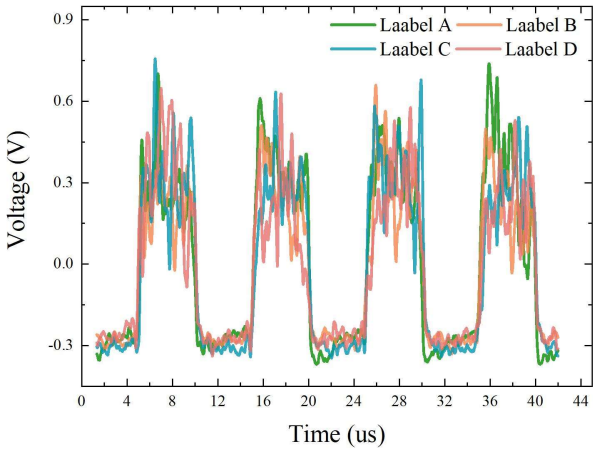

Fig. 8. Output voltage with no object at 100 kHz X-ray pulses.

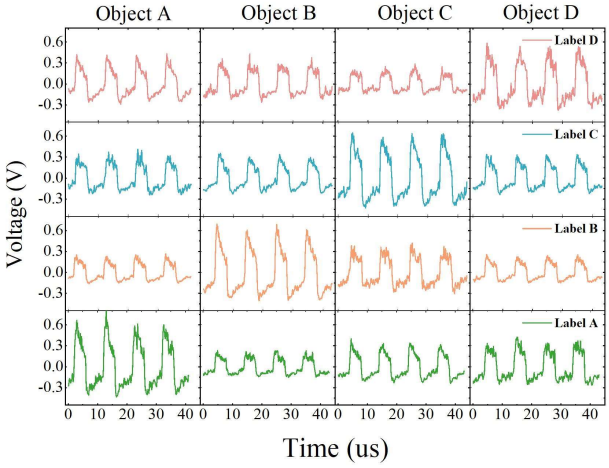

Fig. 9. Output voltage of different objects from 4 SiPM channels for 100 kHz X-ray pulses.

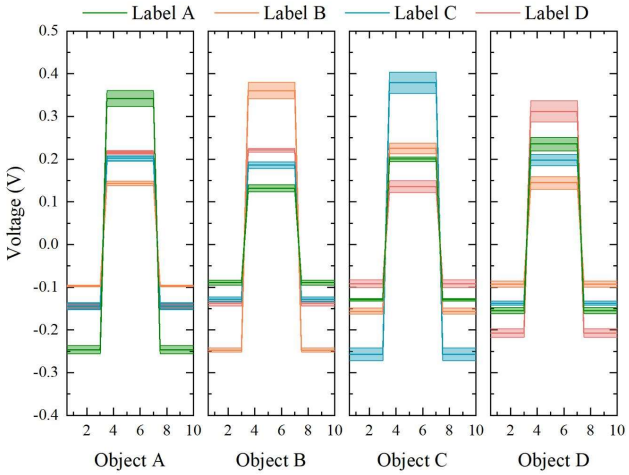

Fig. 10. Average amplitude of 50 groups of signals with different objects for 100 kHz X-ray pulses.

signal was connected to the oscilloscope for observation or storage, and the recognition result could be judged according to the generated signal amplitude. The relative experiment setup is shown in figure 7.

The four output signals are represented by four colored lines of green, yellow, blue, and pink respectively. Each output signal represented one of the four classification labels *A*, *B*, *C*, and *D*. The X-ray tube needs to load the grid-controlled voltage signal when generating pulsed X-rays. In this experiment, the rectangular wave with an amplitude of -5 V and duty cycle of 50% was used, and the waveform was generated by a signal generator. When no object was added, the four signals generated a uniform square wave signal with almost the same amplitude under pulsed X-ray, as shown in figure 8. When an object was placed in front of the X-ray image recognition detector, the output signal of the corresponding channel was obviously higher than that of the other three channels, which could reach above 0.9 V, while the other signal amplitudes were between 0.4 and 0.6 V. The signal can be selected more conveniently by a signal comparator. The X-ray pulse frequency used in figure 9 was 100 kHz, which meant the time to realize a single object recognition was 10 us, and the image recognition speed of 100,000 frames per second could be realized. The waveform detected by the actual detector shown in the figure is somewhat different from the square wave because the X-ray signal has overshoot at a lower rate. To show the results more clearly and to prove the effectiveness of RPNN, 50 groups of signal waveforms under each image are counted, as is shown in figure 10. This figure shows the average amplitude of each signal. It is obtained by calculating the integral value between each signal and the voltage of zero, and then dividing it by the signal width. The broadening of the signal height represents the fluctuation of signals. It can be seen that the signal of the channel which corresponds to the object is obviously higher than that of the other three and it can be clearly distinguished. It proves that the RPNN can realize the function of the neural network. The fluctuation of object D is the most serious, which may be influenced by circuit manufacturing.

When the X-ray pulse frequency increased to 500 kHz, the signal was a little bit distorted. This was because the signal width after the preamplifier and filter was about 800 ns, and the width of the X-ray pulse was 1000 ns, resulting in only one or two X-ray signals consisted the waveform. The square wave signal was composed of multiple X-ray pulse signals, the more X-ray signals there are within each flat top of the wave, the closer the signal tends towards a square wave. Another reason was the non-single energy X-rays produced by the X-ray tube caused statistical fluctuations in the signal. However, the object could still be clearly judged from this signal. The recognition speed at this time, as shown in figure 11, was 500,000 frames per second.

At a pulse frequency of 800 kHz, the signal had serious distortion and obvious amplitude fluctuation. At this frequency, the complete square wave signal could not be output by the preamp and filter signal, which brought a certain probability of misjudgment to the recognition result. This difference was mainly affected by the width of the output signal. The signal reading and measuring device were far apart from each other in the experiment, thus, the signal width was further widened after the necessary amplifier was added. The increase in X-ray pulse frequency should not exceed the minimum width of the SiPM signal. Otherwise, the statistical fluctuation between signals would bring great error to the result, as shown in figure 12.

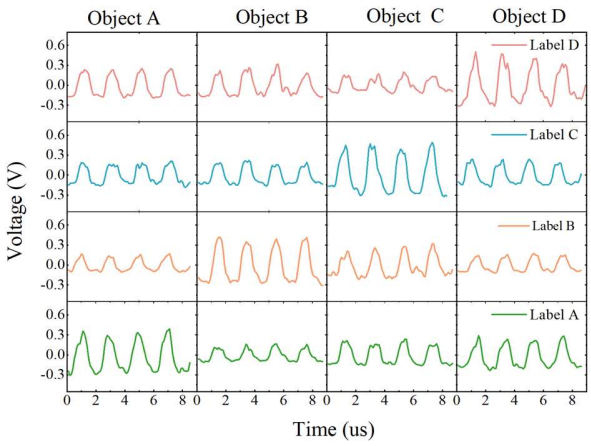

Fig. 11. Output voltage of different objects from 4 SiPM channels for 500 kHz X-ray pulses.

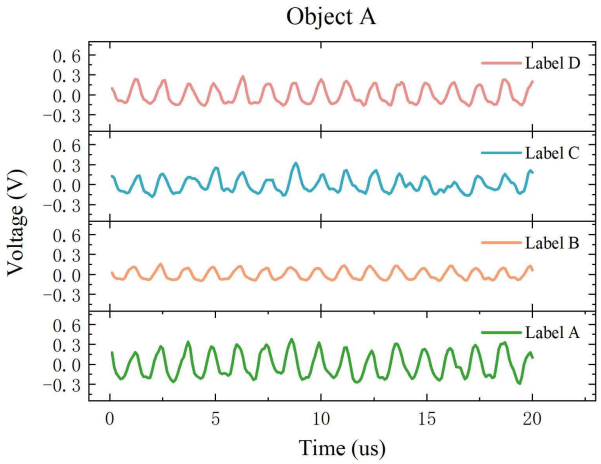

Fig.12. Output voltage from 4 SiPM channels for 800 kHz X-ray pulses for object A.

V. Conclusion and Discussion

In this work, we propose a novel RPNN based on SiPM for high-speed real-time X-ray image recognition. A complete detector system for method verification, including an X-ray emission device, collimation structure, objects, and detection array was independently built. With the existing experiment conditions, the image recognition speed of 500,000 fps can be achieved. This method is different from traditional X-ray imaging. Its structure shows that the recognition speed is not affected by the image resolution in principle, because RPNN has the ability to process all pixels at the same time, instead of serial pixel processing in traditional computer system. Under this simple experimental condition, it has the image processing speed equivalent to the most advanced X-ray imaging at present. At the same time, it can monitor the X-ray images and feed back the shape information of the images in real-time. The response width of the current SiPM output signal was less than 200 ns (from the official datasheet (Hamamatsu S13361 Series)), which means that the theoretical image recognition speed can reach 5 million frames per second. If the synchrotron radiation light source and faster signal amplifier are used, we believe it will have better experimental results.

Here, the classification model also plays a role in reducing the amount of output data, because the classification network can output the key features (image recognition results) of the image. So, for the RPNN detector, it only outputs the key features of the original images and discards the useless information. Subsequent data processing device only needs to process these data with key features (image recognition results) to improve processing efficiency and solve the problem of data explosion. At present, four output channels represent four kinds of recognition images. Theoretically, M outputs can represent 2^M-1 images at most if binary coding is adopted, and when M = 4×4, 65535 kinds of image recognition can be realized.

To improve the spatial resolution, we need to use SiPM with smaller pixels and now there is micron-level SiPM under study [25]. In terms of algorithm, studies have shown that the 784 input and10 output network with a total of 7840 pixels can achieve an accuracy rate of 90.5% for MNIST handwritten data sets [21], which verified the effectiveness of this structured network in the face of more complex images and actual situations.

The main purpose of this paper is to verify the feasibility of this method on SiPM. Although the experimental conditions are relatively simple, it is enough to prove the function. Compared with the current advanced high-speed X-ray imaging detector, it has the advantages of a fast speed and uninterrupted real-time image information feedback. This characteristic indicates that it has unique advantages for some specific applications that only focus on the results but not on the image itself. For example, in online monitoring of laser processing, methods such as sound, ultrasonic, and image are mainly used at present [8][9][26]. Among them, image is the only direct observation method, but this method has strict requirements for the location of sensors and light sources [27], and it can't observe the processing phenomenon inside materials. X-ray imaging can observe phenomenon inside of materials but is typically only used for offline analysis. So, the RPNN is foreseen to have great application potential in the long-term monitoring of X-ray images and quick feedback of results [27][28].

References

[1] R. Cunningham *et al.*, "Keyhole threshold and morphology in laser melting revealed by ultrahigh-speed x-ray imaging," *Science (80-.).*, vol. 363, no. 6429, pp. 849–852, 2019.

[2] N. D. Parab *et al*., "Real time observation of binder jetting printing process using high-speed X-ray imaging," *Sci. Rep.*, vol. 9, no. 1, pp. 1–10, 2019.

[3] D. P. Finegan *et al.*, "In-operando high-speed tomography of lithium-ion batteries during thermal runaway," *Nat. Commun.*, vol. 6, pp. 1–10, 2015.

[4] J. F. De Palma and J. L. Gelet, "Observation of arcing inside a fuse under capacitor-discharge using 1 million frames per second X-ray imaging," *2017 19th Eur. Conf. Power Electron. Appl. EPE 2017 ECCE Eur.*, vol. 2017-Janua, pp. 1–10, 2017.

[5] S. Miller *et al.*, "Ultrahigh-speed X-ray imaging of hypervelocity projectiles," *Nucl. Instruments Methods Phys. Res. Sect. A Accel. Spectrometers, Detect. Assoc. Equip.*, vol. 648, no. SUPPL. 1, pp. S293–S296, 2011.

[6] M. P. Olbinado *et al.*, "Advances in indirect detector systems for ultra high-speed hard X-ray imaging with synchrotron light," *J. Instrum.*, vol. 13, no. 4, 2018.

[7] C. Hu *et al.*, "Ultrafast inorganic scintillator-based front imager for Gigahertz Hard X-ray imaging," *Nucl. Instruments Methods Phys. Res.*

Sect. A Accel. Spectrometers, Detect. Assoc. Equip., vol. 940, no. March, pp. 223–229, 2019.

[8] J. Wu, X. Liu, J. Zhao, H. Qiao, Y. Zhang, and H. Zhang, "The online monitoring method research of laser shock processing based on Plasma Acoustic Wave Signal Energy," *Optik,* vol. 183, pp. 1151–1159, 2019.

[9] Y. Zhang, X. Wang, Q. Yang, R. Xue, J. Zhang, Y. Sun, D. Xu, and S. Krishnaswamy, "Research on epoxy resin curing monitoring using laser ultrasonic," *Measurement,* vol. 158, p. 107737, 2020.

[10] Kong, Quan, *et al.*, "Multimodal Deep Neural Networks Based Ensemble Learning for X-Ray Object Recognition," *Computer Vision–ACCV 2018 Workshops: 14th Asian Conference on Computer Vision, Perth, Australia, December 2–6, 2018, Revised Selected Papers 14.* Springer International Publishing, 2019.

[11] Xiao Z, Song K Y, Gupta M M, "Development of a CNN edge detection model of noised X-ray images for enhanced performance of non-destructive testing," *Measurement,* vol. 174, p. 109012, 2021.

[12] H. T. Philipp, M. W. Tate, P. Purohit, K. S. Shanks, J. T. Weiss, and S. M. Grunera, "High-speed X-ray imaging pixel array detector for synchrotron bunch isolation," *J. Synchrotron Radiat.*, vol. 23, no. 2, pp. 395–403, 2016.

[13] H. T. Philipp *et al.*, "High-speed x-ray imaging with the Keck pixel array detector (Keck PAD) for time-resolved experiments at synchrotron sources," *AIP Conf. Proc.*, vol. 1741, no. July, 2016.

[14] H. T. Philipp, M. W. Tate, K. S. Shanks, P. Purohit, and S. M. Gruner, "Practical considerations for high-speed X-ray pixel array detectors and X-ray sensing materials," *Nucl. Instruments Methods Phys. Res. Sect. A Accel. Spectrometers, Detect. Assoc. Equip.*, vol. 925, no. January, pp. 18–23, 2019.

[15] Xie H, Luo H, Du G, *et al*., "High-efficiency fast X-ray imaging detector development at SSRF," *J. Synchrotron Radiat.,* vol. 26.5, pp. 1631-1637, 2019.

[16] Chang, J., Sitzmann, V., Dun, X. *et al*. "Hybrid optical-electronic convolutional neural networks with optimized diffractive optics for image classification," *Sci Rep,* vol. 8, p. 12324, 2018.

[17] Zhou, T., Lin, X., Wu, J. *et al*. "Large-scale neuromorphic optoelectronic computing with a reconfigurable diffractive processing unit," *Nat. Photonics,* vol. 15, pp. 367–373, 2021.

[18] C. Posch, T. Serrano-Gotarredona, B. Linares-Barranco, and T. Delbruck, "Retinomorphic event-based vision sensors: Bioinspired cameras with spiking output," *Proc. IEEE*, vol. 102, no. 10, pp. 1470–1484, 2014.

[19] C. Choi *et al.*, "Human eye-inspired soft optoelectronic device using high-density MoS2-graphene curved image sensor array," *Nat. Commun.*, vol. 8, no. 1, 2017.

[20] L. Mennel, J. Symonowicz, S. Wachter, D. K. Polyushkin, A. J. Molina-Mendoza, and T. Mueller, "Ultrafast machine vision with 2D material neural network image sensors," *Nature*, vol. 579, no. 7797, pp. 62–66, 2020.

[21] Z. Wang, R. Lin, D. Qu, X. Cui, and P. Tian, "Ultrafast machine vision with artificial neural network devices based on a GaN-based micro-LED array," *Opt. Express*, vol. 29, no. 20, p. 31963, 2021.

[22] P. Eckert, H. C. Schultz-Coulon, W. Shen, R. Stamen, and A. Tadday, "Characterisation studies of silicon photomultipliers," *Nucl. Instruments Methods Phys. Res. Sect. A Accel. Spectrometers, Detect. Assoc. Equip.*, vol. 620, no. 2–3, pp. 217–226, 2010.

[23] D. E. Rumelhart and G. E. Hintont, "Learning Representations by Back-Propagating Errors," *Cogn. Model.*, no. 2, pp. 3–6, 2019.

[24] Z. Feng, Y. Liu, J. Mu, W. Chen, S. Lai, and X. Tang, "Optimization and testing of groove-shaped grid-controlled modulated X-ray tube for X-ray communication," *Nucl. Instruments Methods Phys. Res. Sect. A Accel. Spectrometers, Detect. Assoc. Equip.*, vol. 1026, no. August 2021, p. 166218, 2022.

[25] W. Yue *et al.*, "Performance of ultra-small silicon photomultiplier array with active area of 0.12 mm×0.12 mm," *Nucl. Instruments Methods Phys. Res. Sect. A Accel. Spectrometers, Detect. Assoc. Equip.*, vol. 787, pp. 38–41, 2015.

[26] M. Abdelrahman, E. W. Reutzel, A. R. Nassar, and T. L. Starr, "Flaw detection in powder bed fusion using optical imaging," *Additive Manufacturing,* vol. 15, pp. 1–11, 2017.

[27] Z.-J. Hou *et al.*, "Online Monitoring Technology of Metal Powder Bed Fusion Processes: A Review," *Materials,* vol. 15, no. 21, p. 7598, Oct.2022.

[28] Z. Jiang and J. Wang, "Research status of on-line monitoring of laser metal deposition," *IOP Conf. Ser. Mater. Sci. Eng.*, vol. 605, no. 1, 2019